

Article

## Deformation-Induced Martensitic Transformation in Cu-Zr-Zn Bulk Metallic Glass Composites

Dianyu Wu <sup>1</sup>, Kaikai Song <sup>2,3,\*</sup>, Chongde Cao <sup>1,\*</sup>, Ran Li <sup>4</sup>, Gang Wang <sup>5</sup>, Yuan Wu <sup>6</sup>, Feng Wan <sup>1</sup>, Fuli Ding <sup>1</sup>, Yue Shi <sup>1</sup>, Xiaojun Bai <sup>1</sup>, Ivan Kaban <sup>3,7</sup> and Jürgen Eckert <sup>8,9</sup>

<sup>1</sup> Department of Physics, School of Science, Northwestern Polytechnical University, Youyi Xilu 127, 710072 Xi'an, China; E-Mails: 18740443890@163.com (D.W.); wanfeng1101@163.com (F.W.); dingfuli2008@163.com (F.D.); shiyue@hi123.com (Y.S.); xjbai@nwpu.edu.cn (X.B.)

<sup>2</sup> School of Mechanical, Electrical & Information Engineering, Shandong University (Weihai), Wenhua Xilu 180, 264209 Weihai, China

<sup>3</sup> IFW Dresden, Institute for Complex Materials, Helmholtzstraße 20, 01069 Dresden, Germany; E-Mail: i.kaban@ifw-dresden.com

<sup>4</sup> Key Laboratory of Aerospace Materials and Performance (Ministry of Education), School of Materials Science and Engineering, Beihang University, 100191 Beijing, China; E-Mail: liran@buaa.edu.cn

<sup>5</sup> Laboratory for Microstructures, Shanghai University, 200444 Shanghai, China; E-Mail: g.wang@shu.edu.cn

<sup>6</sup> State Key Laboratory for Advanced Metals and Materials, University of Science and Technology Beijing, 100191 Beijing, China; E-Mail: wuyuan@ustb.edu.cn

<sup>7</sup> TU Dresden, Institut für Werkstoffwissenschaft, 01062 Dresden, Germany

<sup>8</sup> Erich Schmid Institute of Materials Science, Austrian Academy of Sciences, Jahnstraße 12, A-8700 Leoben, Austria; E-Mail: juergen.eckert@unileoben.ac.at

<sup>9</sup> Department Materials Physics, Montanuniversität Leoben, Jahnstraße 12, A-8700 Leoben, Austria

\* Authors to whom correspondence should be addressed;

E-Mails: songkaikai8297@gmail.com (K.S.); caocd@nwpu.edu.cn (C.C.);

Tel.: +86-029-8843-1657 (C.C.); Fax: +86-029-8843-1656 (C.C.).

Academic Editors: K.C. Chan and Jordi Sort Viñas

Received: 23 October 2015 / Accepted: 11 November 2015 / Published: 17 November 2015

---

**Abstract:** The microstructures and mechanical properties of  $(\text{Cu}_{0.5}\text{Zr}_{0.5})_{100-x}\text{Zn}_x$  ( $x = 0, 1.5, 2.5, 4.5, 7, 10,$  and  $14$  at. %) bulk metallic glass (BMG) composites were studied. CuZr martensitic crystals together with minor B2 CuZr and amorphous phases dominate the

microstructures of the as-quenched samples with low Zn additions ( $x = 0, 1.5,$  and  $2.5$  at. %), while B2 CuZr and amorphous phases being accompanied with minor martensitic crystals form at a higher Zn content ( $x = 4.5, 7, 10,$  and  $14$  at. %). The fabricated Cu-Zr-Zn BMG composites exhibit macroscopically appreciable compressive plastic strain and obvious work-hardening due to the formation of multiple shear bands and the deformation-induced martensitic transformation (MT) within B2 crystals. The present BMG composites could be a good candidate as high-performance structural materials.

**Keywords:** metallic glasses; composites; rapid solidification; martensitic transformation

---

## 1. Introduction

Although bulk metallic glasses (BMGs) exhibit attractive mechanical properties, such as high strength, high hardness, and a large elastic strain limit, they usually fail in an apparently brittle manner during deformation at room temperature [1–6]. A poor ductility, caused by shear localization and strain/thermal softening, severely restricts their practical applications as structural and functional materials [1–6]. In order to circumvent this shortcoming, BMG composites with ductile crystals precipitating in the glassy matrix have been developed in various alloy systems by *in situ* and *ex situ* fabrication methods [5–9]. It has been reported that improved toughness, and even tensile ductility, can be observed in such BMG composites by properly adjusting compositions, microstructures, and casting methods [5–18]. During deformation at room temperature, ductile crystals can effectively suppress the rapid propagation of the main shear bands and induce the formation of multiple shear bands in the glassy matrix [5–18]. However, these ductile crystals during deformation cannot provide sufficient work-hardening to eliminate the work-softening effect induced by the formation of shear bands in the glassy matrix, resulting in the microscopic strain-softening of BMG composites [10–18].

Recently, it has been found that, by introducing a shape memory ductile phase into the glassy matrix, the fabricated BMG composites show not only a pronounced tensile ductility but also a macroscopic work-hardening capability during deformation at room temperature [19–27]. Upon loading, besides the formation of multiple shear bands in the glassy matrix, ductile shape memory crystals experience the martensitic transformation (MT) from a cubic phase to monoclinic phases [19–27], which can provide the pronounced work hardening. Hence, the weakness of the work-softening effect during deformation of BMG composites can be effectively overcome.

Until now, CuZr- and TiNiCu-based alloy systems with different compositions have been fabricated into BMG composites [19–28]. For example, CuZr-based BMG composites with different sample sizes containing minor element additions such as Al, Ti, Ag, Ni, Co, Y, Er, V, W, or Ta have been successfully fabricated [20–25,29–37]. Two key requirements should be satisfied for the fabrication of CuZr-based BMG composites: (1) maintaining sufficiently high glass-forming ability (GFA) in order to fabricate large-sized BMG composites [20–25,29–37]; and (2) stabilization of metastable B2 CuZr phase in order to suppress its decomposition into equilibrium phases (EPs) [29–34]. Previous results [22,38] demonstrated that minor Co addition to CuZr alloys can dramatically enhance the thermal stability of the B2 CuZr phase but gravely deteriorate the GFA of CuZr-based alloys. Our

recent work [39] has shown that minor Zn addition to binary CuZr alloys can not only improve their GFA but also effectively stabilize the B2 CuZr phase to low temperatures. Additionally, as a rule of thumb, Zn is much cheaper than Co, Al, Ag, Ti, Hf, or rare earth metals. Therefore, it is beneficial to fabricate Cu-Zr-Zn BMG composites and further investigate the correlation between microstructures and mechanical properties of Cu-Zr-Zn BMG composites. In this paper, the microstructures and mechanical properties of  $(\text{Cu}_{0.5}\text{Zr}_{0.5})_{100-x}\text{Zn}_x$  ( $x = 0, 2.5, 4.5, 7, 10,$  and  $14$  at. %) BMG composites were investigated. Furthermore, the corresponding deformation mechanism at room temperature of Cu-Zr-Zn BMG composites was also discussed.

## 2. Experimental Section

$\text{Cu}_{50}\text{Zr}_{50}$  master alloys were prepared by arc-melting appropriate amounts of the constituting elements (at least purity 99.9%) under a Ti-gettered argon atmosphere. Each ingot was remelted at least three times in order to achieve chemical homogeneity. Afterwards, master alloys with nominal compositions of  $(\text{Cu}_{0.5}\text{Zr}_{0.5})_{100-x}\text{Zn}_x$  ( $x = 0, 1.5, 2.5, 4.5, 7, 10,$  and  $14$  at. %) were melted using a high frequency furnace under an argon atmosphere. They were then cast into rods with a diameter of 2 mm using an injection casting machine. The microstructures of the as-cast samples were characterized using an optical microscope (OM, Olympus, Tokyo, Japan) and X-ray diffraction (XRD) in reflection geometry (Rigaku D/max-rB). The XRD measurements were performed on longitudinal sections of four polished rods with a final dimension of about  $2 \text{ mm} \times 5 \text{ mm} \times 0.7 \text{ mm}$ . Room-temperature compression tests were performed on specimens with a diameter of about  $\text{Ø}2 \text{ mm}$  and a height of 4 mm using an electronic universal testing machine (New SANS, MTS System Corporation (China), Shenzhen, China) at an initial strain rate of  $2.5 \times 10^{-4} \cdot \text{s}^{-1}$ . The microstructures of the as-cast rods after deformation were checked using a scanning electron microscope (SEM) and XRD, respectively.

## 3. Results and Discussion

### 3.1. Phase Formation in the As-Cast Cu-Zr-Zn Rods

Figure 1 shows XRD patterns of the as-cast  $(\text{Cu}_{0.5}\text{Zr}_{0.5})_{100-x}\text{Zn}_x$  ( $x = 0, 1.5, 2.5, 4.5, 7, 10,$  and  $14$  at. %) rods. For the samples with low Zn contents of 0, 1.5, and 2.5 at. %, the dominating phase is CuZr martensite, being similar to previous reports [19–27]. Additionally, a small quantity of B2 CuZr phase being accompanied with minor  $\text{Cu}_{10}\text{Zr}_7$  crystals can be observed in the matrix. With Zn content increasing to 4.5 and 7 at. %, the volume fractions of CuZr martensitic crystals decrease quickly, while a large number of B2 CuZr crystals ( $Pm-3m$ ) precipitate [40–42]. However, it is difficult to conclude on the existence of amorphous phase due to much higher peak intensities of crystals than those of the amorphous phase for the as-cast  $(\text{Cu}_{0.5}\text{Zr}_{0.5})_{100-x}\text{Zn}_x$  ( $x = 0, 1.5,$  and  $2.5$  at. %) samples. Meanwhile, for the Cu-Zr-Zn samples with 10 and 14 at.% Zn additions, a broad diffraction hump around  $2\theta = 38.5^\circ$  in the XRD patterns corresponding with amorphous phase is clearly seen together with crystalline reflexes of B2 CuZr and martensitic crystals in Figure 1. These observations reveal that minor Zn addition effectively improves the GFA of CuZr-based alloys. Recently, by using *in situ* high-accuracy X-ray diffraction analysis on  $\text{Cu}_{50}\text{Zr}_{50}$  MG, Kalay *et al.* found that only the B2 CuZr phase is observed at 1045 K while at 1002 K a mixture of B2 CuZr,  $\text{Cu}_{10}\text{Zr}_7$ , and  $\text{CuZr}_2$  crystals appear [43]. With

decreasing temperature to 789 K,  $\text{Cu}_{10}\text{Zr}_7$  and  $\text{CuZr}_2$  crystals can be found, which further confirms previous *ex situ* experimental results [30,31,34]. Therefore, during quenching of Cu-Zr-Zn melts, the B2 CuZr phase should be kept to room temperature. However, MT would be induced within some B2 CuZr crystals due to the thermal stress originating from rapid quenching [29,41], resulting in the precipitation of monoclinic martensitic crystals. It has been shown that monoclinic martensitic phases consist of two kinds of structures, *i.e.*, basic structure (B19',  $P2_1/m$ ) and superstructures (B33, Cm) [40–42]. In our case, since Zn addition can also stabilize B2 CuZr phase to low temperatures [39], a larger number of B2 CuZr crystals could be obtained with Zn content increasing. On the other hand, the eutectoid decomposition of the B2 CuZr phase into other EPs can also be inhibited to some extent [39] since the thermal stability of the B2 CuZr phase is enhanced with the addition of Zn. That would result in the decrease of the volume fraction of  $\text{Cu}_{10}\text{Zr}_7$  crystals in the matrix with Zn content increasing from 0 at. % to 14 at. %. As a result, martensitic crystals, B2 CuZr phase, amorphous phase, and/or a little  $\text{Cu}_{10}\text{Zr}_7$  crystals can be obtained during solidification, ultimately resulting in the formation of Cu-Zr-Zn BMG composites.

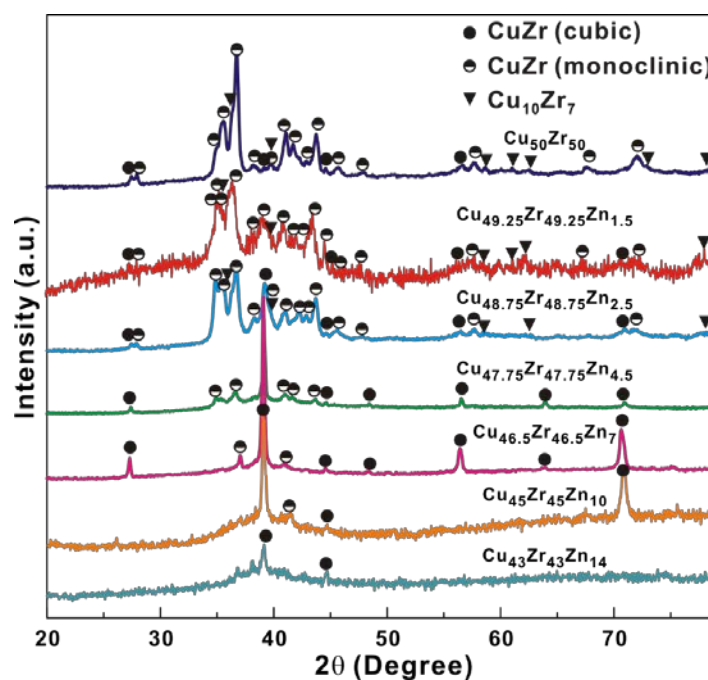


**Figure 1.** XRD patterns of the as-cast  $(\text{Cu}_{0.5}\text{Zr}_{0.5})_{100-x}\text{Zn}_x$  ( $x = 0, 1.5, 2.5, 4.5, 7, 10,$  and  $14$  at. %) rods with a diameter of 2 mm.

In order to further illustrate the phase formation in the as-quenched CuZr-based alloys with Zn additions, the corresponding OM pictures are presented in Figure 2. In the  $(\text{Cu}_{0.5}\text{Zr}_{0.5})_{100-x}\text{Zn}_x$  ( $x = 0, 1.5,$  and  $2.5$  at. %) samples, obvious martensitic plates were found in the matrix (marked by the red arrows in Figure 2a–c). Additionally, a little amorphous phase appears around the outer regions of the as-cast rods (marked by the blue dotted arrows in Figure 2a–c) due to a relatively higher cooling rate. For the as-cast  $\text{Cu}_{47.25}\text{Zr}_{47.25}\text{Zn}_{4.5}$  sample, a large volume fraction of the B2 CuZr phase within the glassy matrix can be observed (see the red dot-dashed arrows in Figure 2d). Moreover, as it is seen in the insets in Figure 2d, some martensitic plates also appear within the B2 CuZr crystals. With increasing Zn content from 7 at. % to 10 at. %, the volume fraction of the B2 CuZr phase decreases while that of

the amorphous phase gradually increases (Figure 2e,f). As it is shown in Figure 2f,g, the bottom and top parts of the  $\text{Cu}_{45}\text{Zr}_{45}\text{Zn}_{10}$  rod consist of amorphous and crystalline phases. The corresponding volume fractions of the crystals at the bottom parts of the as-cast rods were less than those of the top parts due to somewhat different cooling rates. Furthermore, for the  $\text{Cu}_{43}\text{Zr}_{43}\text{Zn}_{14}$  rod, the XRD pattern of the middle and top parts show a nature of BMG composites (Figure 1) while the bottom parts are fully amorphous from the OM images shown in Figure 2h. The differences for the volume fractions of amorphous phase between  $\text{Cu}_{45}\text{Zr}_{45}\text{Zn}_{10}$  and  $\text{Cu}_{43}\text{Zr}_{43}\text{Zn}_{14}$  rods should be contributed to the increase of GFA with Zn content increasing. In order to further ascertain heterogeneous distributions of the B2 CuZr crystals in the glassy matrix, OM measurements were performed on the longitudinal cross-sections of the as-cast  $\text{Cu}_{48.75}\text{Zr}_{48.75}\text{Zn}_{2.5}$  rod. As shown in Figure 3a,b, almost fully crystalline microstructures are observed at the top parts of the investigated sample, whereas the bottom parts (Figure 3c,d) contain a larger fraction of the amorphous phase. Nevertheless, the changes of the volume fraction of the amorphous phase for the top part to bottom part in same rods reveal that the differences in the applied cooling rates may induce either vitrification or precipitation of crystals.

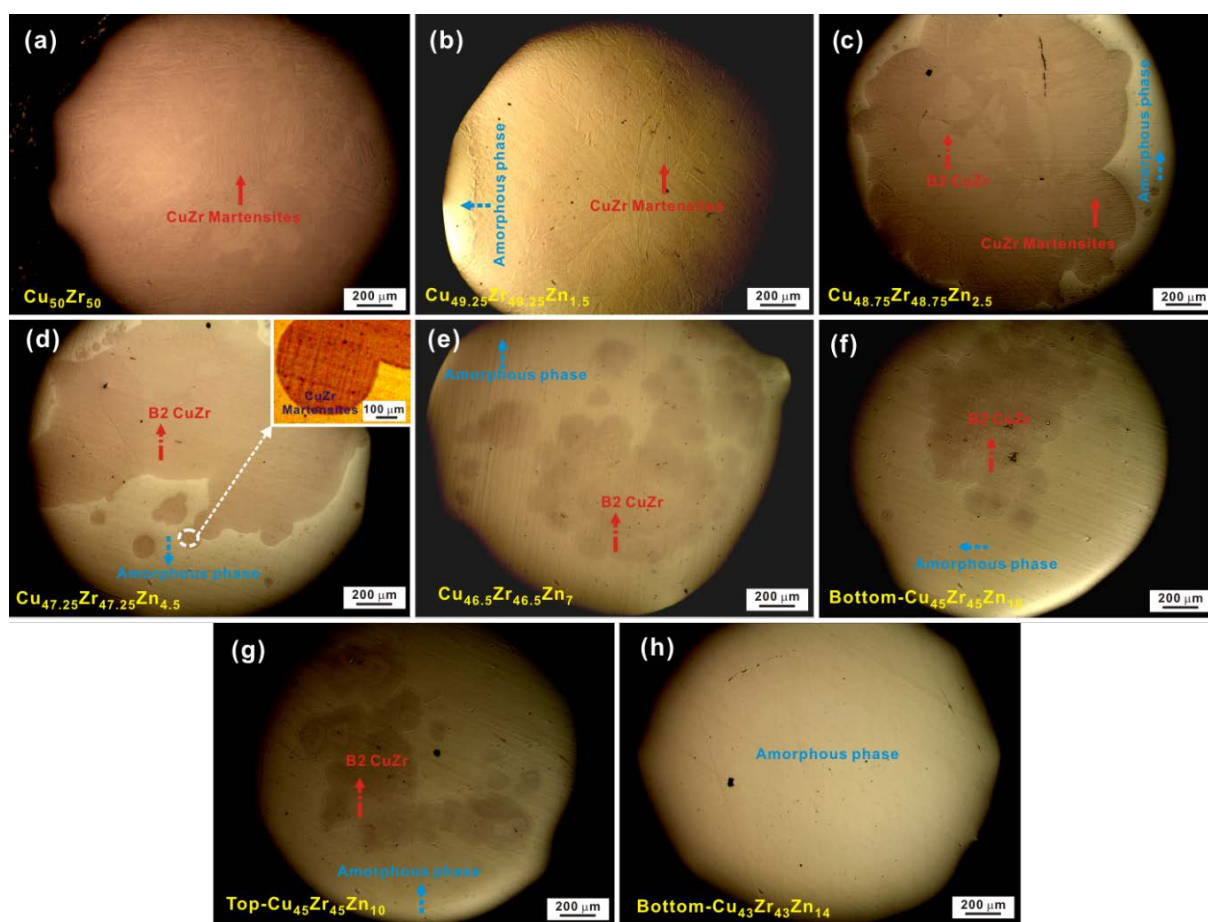


**Figure 2.** OM pictures of the as-cast  $(\text{Cu}_{0.5}\text{Zr}_{0.5})_{100-x}\text{Zn}_x$  ( $x =$  (a) 0; (b) 1.5 at. %; (c) 2.5 at. %; (d) 4.5 at. %; (e) 7 at. %; (f,g) 10 at. %; and (h) 14 at. %) rods with a diameter of 2 mm [39]; Inset: martensitic plates within B2 CuZr crystals.

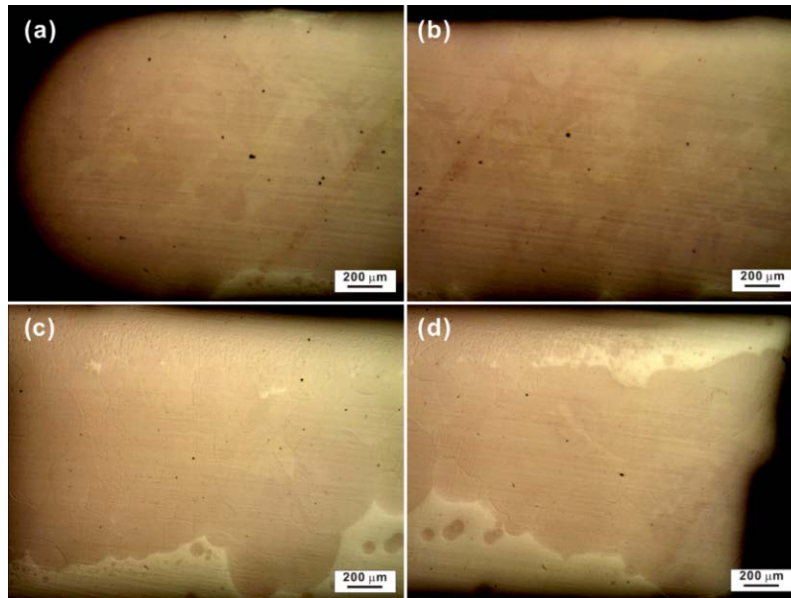


**Figure 3.** OM pictures of the longitudinal cross-sections cut from the top parts (a,b) to from the bottom parts (c,d) of the as-cast  $\text{Cu}_{48.75}\text{Zr}_{48.75}\text{Zn}_{2.5}$  rod; The neighboring microstructures from the top parts and the bottom parts from a same rod were shown in Figure 3a,b and Figure 3c,d, respectively.

### 3.2. Mechanical Properties of the As-Cast Cu-Zr-Zn Samples

Figure 4 exhibits the strain-stress curves measured upon uniaxial compression at room temperature for the as-cast Cu-Zr-Zn rods. It has been reported that the yield stresses of the B2 CuZr phase and CuZr martensitic crystals are lower than 500 MPa while these of CuZr-based BMGs are higher than 1700 MPa [13,17,20–27]. Hence, with increasing volume fraction of the amorphous phase, as shown in Figure 4, the yield stress increases gradually. As shown in Figure 4a, the as-cast  $(\text{Cu}_{0.5}\text{Zr}_{0.5})_{100-x}\text{Zn}_x$  ( $x = 0$  and 2.5 at. %) rods show a similar compressive curves to CuZr martensites [21,24] since martensitic crystals dominate their microstructures. Their average yield stress is  $819 \pm 60$  MPa and  $839 \pm 200$  MPa, while their fracture strength is  $1821 \pm 75$  MPa and  $1772 \pm 120$  MPa, respectively (Figure 4a and Table 1). Furthermore, with Zn content increasing from 4.5 at. % to 7 at. %, the average yield stress and average fracture stress increase from  $830 \pm 220$  MPa to  $906 \pm 115$  MPa,  $1713 \pm 75$  MPa, and  $1884 \pm 60$  MPa, respectively. Meanwhile, an average plastic strain of  $6.8\% \pm 0.8\%$  and  $6.6\% \pm 0.8\%$  can be obtained for both of samples, respectively (Figure 4b and Table 1). As mentioned in Section 3.1, the as-cast  $(\text{Cu}_{0.5}\text{Zr}_{0.5})_{100-x}\text{Zn}_x$  ( $x = 4.5$  and 7 at. %) samples mainly consist of B2 CuZr crystals and amorphous phase. Hence, as listed in Table 1, the differences of mechanical properties for top and bottom parts for a same rod are not very obvious.

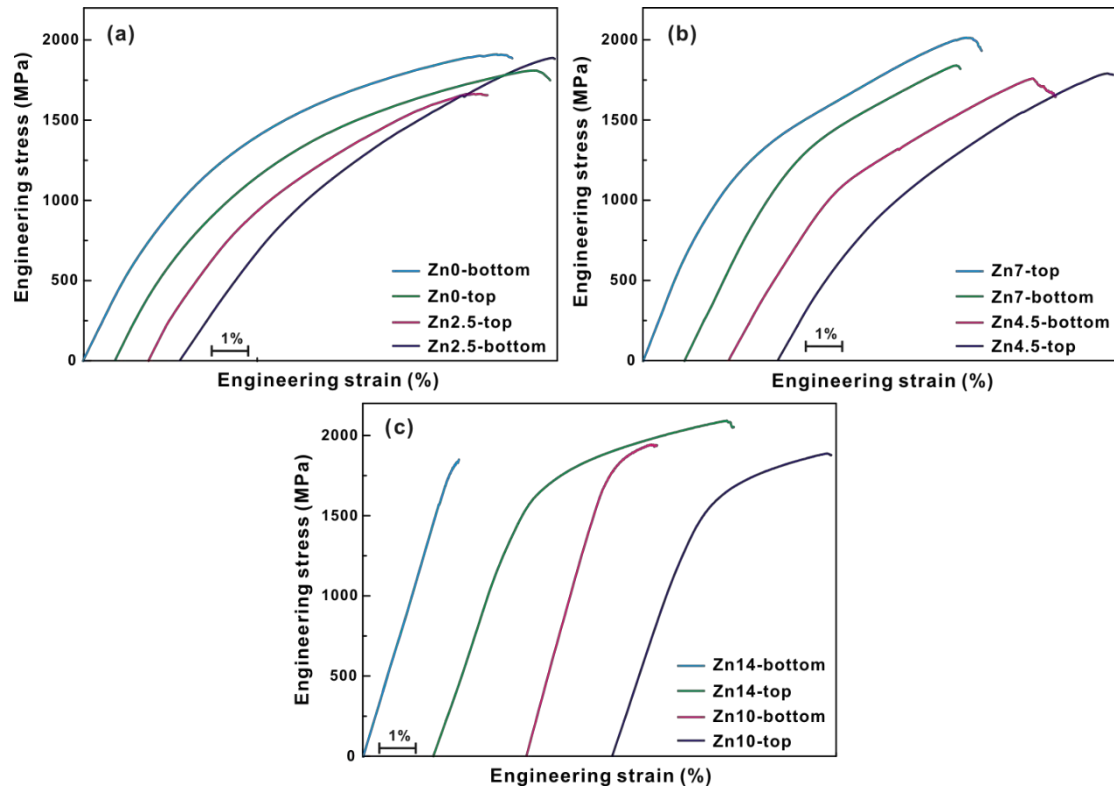


**Figure 4.** Compressive strain-stress curves of the as-cast  $(\text{Cu}_{0.5}\text{Zr}_{0.5})_{100-x}\text{Zn}_x$  rods with a diameter of 2 mm: (a)  $x = 0$  and 2.5 at. %, (b)  $x = 4.5$  and 7 at. %, and (c)  $x = 10$  and 14 at. %; Compressive curves of the top and bottom parts of the as-cast rods were blue and green curves, respectively.

**Table 1.** Yield strength, fracture strength, and plastic strain of different  $(\text{Cu}_{0.5}\text{Zr}_{0.5})_{100-x}\text{Zn}_x$  ( $x = 0, 2.5, 4.5, 7, 10,$  and  $14$  at. %) BMGs and composites.

Samples	Yield Strength (MPa)	Fracture Strength (MPa)	Plastic Strain (%)	Average Yield Strength (MPa)	Average Fracture Strength (MPa)	Average Plastic Strain (%)																																																				
Zn0-Top	$770 \pm 10$	$1752 \pm 10$	$10.0 \pm 0.2$	$819 \pm 60$	$1821 \pm 75$	$9.7 \pm 0.2$																																																				
Zn0-Bottom	$820 \pm 10$	$1821 \pm 10$	$9.7 \pm 0.2$				Zn2.5-Top	$834 \pm 10$	$1646 \pm 10$	$6.8 \pm 0.2$	$839 \pm 200$	$1772 \pm 120$	$7.7 \pm 0.5$	Zn2.5-Bottom	$843 \pm 10$	$1892 \pm 10$	$8.2 \pm 0.2$	Zn4.5-Top	$781 \pm 10$	$1783 \pm 10$	$6.9 \pm 0.2$	$830 \pm 220$	$1713 \pm 75$	$6.8 \pm 0.8$	Zn4.5-Bottom	$1058 \pm 10$	$1643 \pm 10$	$6.0 \pm 0.5$	Zn7-Top	$860 \pm 10$	$1932 \pm 10$	$7.6 \pm 0.5$	$906 \pm 115$	$1884 \pm 60$	$6.6 \pm 0.8$	Zn7-Bottom	$1086 \pm 10$	$1819 \pm 10$	$5.0 \pm 0.5$	Zn10-Top	$1420 \pm 10$	$1881 \pm 10$	$3.7 \pm 0.5$	$1515 \pm 200$	$1906 \pm 100$	$2.8 \pm 1.2$	Zn10-Bottom	$1773 \pm 10$	$1940 \pm 10$	$1.2 \pm 0.5$	Zn14-Top	$1464 \pm 10$	$2051 \pm 10$	$6.0 \pm 0.5$	$1636 \pm 200$	$1943 \pm 100$	$3 \pm 3$	Zn14-Bottom
Zn2.5-Top	$834 \pm 10$	$1646 \pm 10$	$6.8 \pm 0.2$	$839 \pm 200$	$1772 \pm 120$	$7.7 \pm 0.5$																																																				
Zn2.5-Bottom	$843 \pm 10$	$1892 \pm 10$	$8.2 \pm 0.2$				Zn4.5-Top	$781 \pm 10$	$1783 \pm 10$	$6.9 \pm 0.2$	$830 \pm 220$	$1713 \pm 75$	$6.8 \pm 0.8$	Zn4.5-Bottom	$1058 \pm 10$	$1643 \pm 10$	$6.0 \pm 0.5$	Zn7-Top	$860 \pm 10$	$1932 \pm 10$	$7.6 \pm 0.5$	$906 \pm 115$	$1884 \pm 60$	$6.6 \pm 0.8$	Zn7-Bottom	$1086 \pm 10$	$1819 \pm 10$	$5.0 \pm 0.5$	Zn10-Top	$1420 \pm 10$	$1881 \pm 10$	$3.7 \pm 0.5$	$1515 \pm 200$	$1906 \pm 100$	$2.8 \pm 1.2$	Zn10-Bottom	$1773 \pm 10$	$1940 \pm 10$	$1.2 \pm 0.5$	Zn14-Top	$1464 \pm 10$	$2051 \pm 10$	$6.0 \pm 0.5$	$1636 \pm 200$	$1943 \pm 100$	$3 \pm 3$	Zn14-Bottom	$1815 \pm 10$	$1840 \pm 10$	$0.1 \pm 0.02$								
Zn4.5-Top	$781 \pm 10$	$1783 \pm 10$	$6.9 \pm 0.2$	$830 \pm 220$	$1713 \pm 75$	$6.8 \pm 0.8$																																																				
Zn4.5-Bottom	$1058 \pm 10$	$1643 \pm 10$	$6.0 \pm 0.5$				Zn7-Top	$860 \pm 10$	$1932 \pm 10$	$7.6 \pm 0.5$	$906 \pm 115$	$1884 \pm 60$	$6.6 \pm 0.8$	Zn7-Bottom	$1086 \pm 10$	$1819 \pm 10$	$5.0 \pm 0.5$	Zn10-Top	$1420 \pm 10$	$1881 \pm 10$	$3.7 \pm 0.5$	$1515 \pm 200$	$1906 \pm 100$	$2.8 \pm 1.2$	Zn10-Bottom	$1773 \pm 10$	$1940 \pm 10$	$1.2 \pm 0.5$	Zn14-Top	$1464 \pm 10$	$2051 \pm 10$	$6.0 \pm 0.5$	$1636 \pm 200$	$1943 \pm 100$	$3 \pm 3$	Zn14-Bottom	$1815 \pm 10$	$1840 \pm 10$	$0.1 \pm 0.02$																			
Zn7-Top	$860 \pm 10$	$1932 \pm 10$	$7.6 \pm 0.5$	$906 \pm 115$	$1884 \pm 60$	$6.6 \pm 0.8$																																																				
Zn7-Bottom	$1086 \pm 10$	$1819 \pm 10$	$5.0 \pm 0.5$				Zn10-Top	$1420 \pm 10$	$1881 \pm 10$	$3.7 \pm 0.5$	$1515 \pm 200$	$1906 \pm 100$	$2.8 \pm 1.2$	Zn10-Bottom	$1773 \pm 10$	$1940 \pm 10$	$1.2 \pm 0.5$	Zn14-Top	$1464 \pm 10$	$2051 \pm 10$	$6.0 \pm 0.5$	$1636 \pm 200$	$1943 \pm 100$	$3 \pm 3$	Zn14-Bottom	$1815 \pm 10$	$1840 \pm 10$	$0.1 \pm 0.02$																														
Zn10-Top	$1420 \pm 10$	$1881 \pm 10$	$3.7 \pm 0.5$	$1515 \pm 200$	$1906 \pm 100$	$2.8 \pm 1.2$																																																				
Zn10-Bottom	$1773 \pm 10$	$1940 \pm 10$	$1.2 \pm 0.5$				Zn14-Top	$1464 \pm 10$	$2051 \pm 10$	$6.0 \pm 0.5$	$1636 \pm 200$	$1943 \pm 100$	$3 \pm 3$	Zn14-Bottom	$1815 \pm 10$	$1840 \pm 10$	$0.1 \pm 0.02$																																									
Zn14-Top	$1464 \pm 10$	$2051 \pm 10$	$6.0 \pm 0.5$	$1636 \pm 200$	$1943 \pm 100$	$3 \pm 3$																																																				
Zn14-Bottom	$1815 \pm 10$	$1840 \pm 10$	$0.1 \pm 0.02$																																																							

When the volume fraction of the amorphous phase is close to or larger than 50 vol. %, which was approximately estimated based on the area ratio of the amorphous and crystalline phases extracted

from the OM images [21], the corresponding yield stresses of the as-cast  $(\text{Cu}_{0.5}\text{Zr}_{0.5})_{100-x}\text{Zn}_x$  ( $x = 10$  and 14 at. %) rods become relatively higher (Table 1). As shown in Figure 4c, an average plastic strain of  $2.8\% \pm 1.2\%$  can be achieved for the present  $\text{Cu}_{45}\text{Zr}_{45}\text{Zn}_{10}$  rods. Moreover, due to the inhomogeneous distributions of B2 CuZr phase in the glassy matrix mentioned in the Section 3.1, the mechanical properties of Cu-Zr-Zn rods are extremely different, especially for the samples quenched at a cooling rate approaching the critical cooling rate for the fully amorphous phase. As the content of Zn is 10 at. %, the bottom parts show a high yield strength of  $1773 \pm 10$  MPa together with a small plastic strain of  $1.2\% \pm 0.5\%$ , while the respective values for the top parts are approximately  $1420 \pm 10$  MPa and  $3.7\% \pm 0.5\%$ , respectively. The corresponding fracture strength changes from  $1940 \pm 10$  MPa to  $1881 \pm 10$  MPa. As shown in Figure 4c and listed in Table 1, the bottom parts of the as-cast  $\text{Cu}_{43}\text{Zr}_{43}\text{Zn}_{14}$  rods show a higher yield strength of  $1815 \pm 10$  MPa and a smaller plastic strain of  $0.1\% \pm 0.02\%$ , while the respective values for the top parts are equal to  $1464 \pm 10$  MPa and  $6\% \pm 0.5\%$ , respectively. Meanwhile, the corresponding fracture strength increases from  $1840 \pm 10$  MPa to  $2051 \pm 10$  MPa. Nevertheless, all the present BMG composites exhibit macroscopically-detectable compressive plastic strains and obvious work-hardening.

In order to clarify the deformation mechanisms of Cu-Zr-Zn BMG composites at room temperature, the XRD measurement was conducted on the  $\text{Cu}_{45}\text{Zr}_{45}\text{Zn}_{10}$  rods after deformation (Figure 5). It is obvious that more martensitic crystals appear after fracture compared with the as-cast rod (Figure 1), which indicates that B2 CuZr crystals undergo a MT upon loading. It was shown [20,23,25,44] that B2 CuZr crystals can provide a large plastic strain together with pronounced work hardening, being called the transformation-induced plasticity (TRIP) effect. MT within austenitic B2 CuZr crystals during deformation can remarkably release stress concentrations at the interface between the B2 CuZr phase and the glassy matrix [24,25,45–47]. This means that the applied stress is effectively transferred from the glassy matrix to a ductile B2 CuZr phase during deformation, resulting in the restriction of free volume accumulation and the partial release of the elastic energy stored in whole samples [45–47]. As a result, primary shear bands cannot rapidly traverse through an entire sample but need more energy to drive their continuous movement [24,25,45–47], which requires an external stress to activate shear bands. Previous results have shown that there exists an invariant critical stress for continuous shear banding [47]. In order to further investigate shear banding evolutions and MT behaviors during deformation, SEM measurements were also carried out on external surfaces and fractures of the deformed samples (Figure 6). All the samples exhibit a shear fracture and the compressive fracture angle, *i.e.*, the angle between the fracture surface and the loading direction, is approximately equal to  $40^\circ$ – $45^\circ$ . This implies that the compressive fractures of BMG and their composites do not occur along the plane of the maximum shear stress and, accordingly, does not follow the von Mises criterion [48]. As shown in Figure 6, no obvious shear bands can be observed for the deformed  $\text{Cu}_{49.25}\text{Zr}_{49.25}\text{Zn}_{1.5}$  sample which is almost fully crystalline. At the same time, martensitic plates appeared within B2 crystals (see the red arrow in Figure 6a). For the deformed  $\text{Cu}_{47.25}\text{Zr}_{47.25}\text{Zn}_{4.5}$  sample, not only martensitic plates can be observed within the B2 CuZr phase (see the red arrow and inset in Figure 6b), but also multiple shear bands appeared (see the yellow dotted arrow in Figure 6b). For the fully amorphous  $\text{Cu}_{43}\text{Zr}_{43}\text{Zn}_{14}$  sample, only multiple shear bands can be observed (see the yellow dotted arrows in Figure 6c).

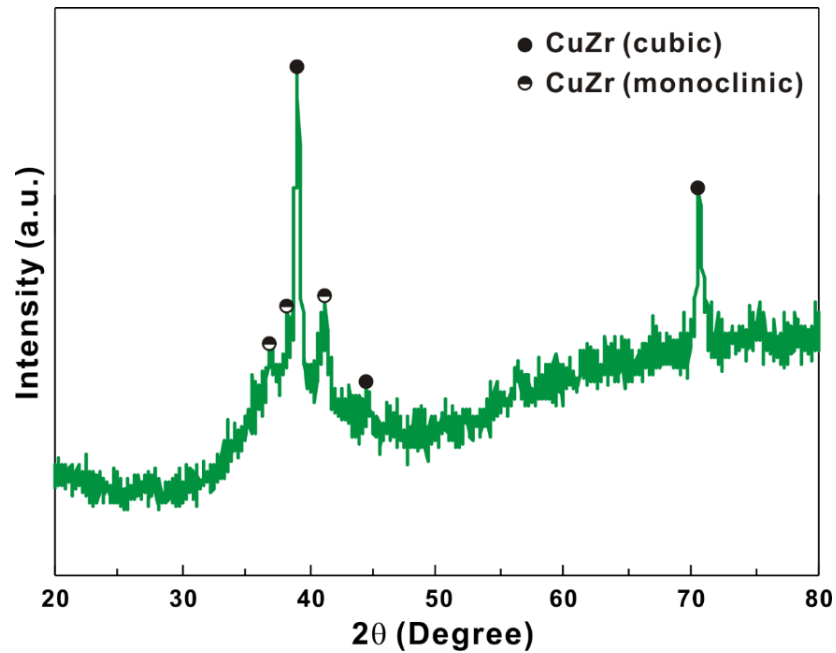


Figure 5. XRD patterns of the as-deformed  $\text{Cu}_{45}\text{Zr}_{45}\text{Zn}_{10}$  rods.

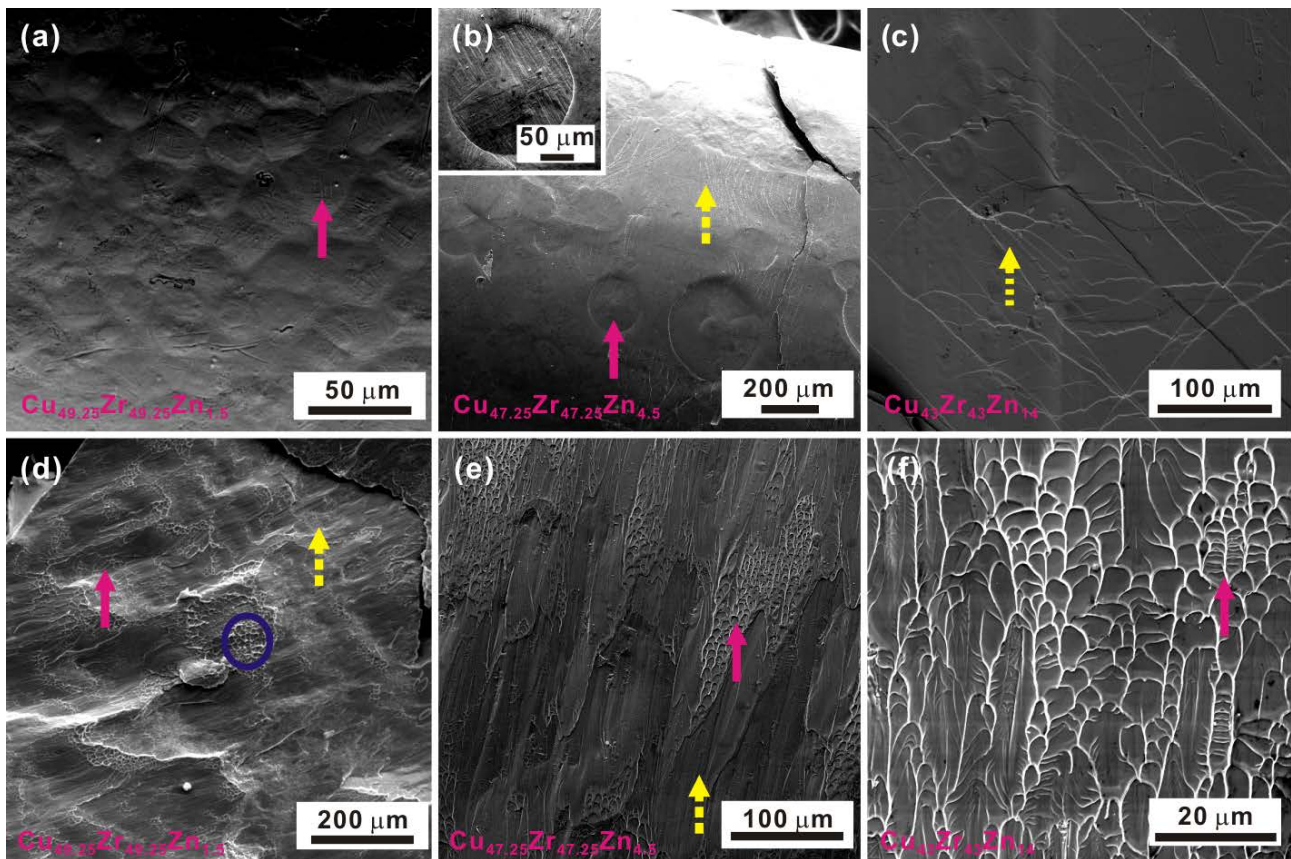


Figure 6. SEM pictures of the external (a–c) and fracture (d–f) surfaces of the deformed  $(\text{Cu}_{0.5}\text{Zr}_{0.5})_{100-x}\text{Zn}_x$  samples: (a)  $x = 1.5$  at. %; (b)  $x = 4.5$  at. %; (c)  $x = 10$  at. %; (d)  $x = 1.5$  at. %; (e)  $x = 4.5$  at. %; and (f)  $x = 14$  at. %. Inset: martensitic plates within the B2 CuZr crystals.

The corresponding fracture images are shown in Figure 6d,f. For almost fully crystalline samples, some slurry-like structures (see the yellow dotted arrows) and dimples were observed (marked by the blue circle) beside a small vein-like structures (see the red arrow in Figure 6d). Cu-Zr-Zn BMG composites after deformation showed not only slurry-like structures but a number of vein- and river-like structures (see the red arrows in Figure 6e, respectively). For the fully amorphous sample, only vein- and river-like structures can be seen (Figure 6f). As we know, fracture surfaces of different BMGs are correlated with their ductility, toughness, deformation rate, and fracture mode [49–52]. Usually, vein-like patterns can be found on the whole fracture surface for BMGs, which is closely related with the significant softening or reduced viscosity in shear bands [49–53]. The origin responsible for the softening has been manifested to be shear-induced structural disordering or temperature rise [49–53]. In our case, by introducing ductile B2 CuZr crystals into the glassy matrix, the MT is quite pronounced during deformation before the formation of shear bands [24,25], resulting in the decrease of the elastic energy density of serration events related with the shear-banding process and then leading to the deceleration of shear-banding [24,25,45,54,55]. Hence, the serration events in the compressive curves become very tiny and almost invisible (Figure 4). Therefore, it is reasonably believed that the second crystals introduced into the glassy matrix could affect the shear-induced structural disordering or temperature rise, resulting in the slightly changes of vein-like patterns. Furthermore, it was shown [56] that typical fracture features of ductile metallic alloys, *i.e.*, dimples, can be observed in ductile samples with pure B2 CuZr crystals. Therefore, for CuZr-based BMG composites, dimples, river- and vein-like patterns were observed. Nevertheless, during deformation, the formation of multiple shear bands, the deformation-induced MT within B2 CuZr crystals, and the interactions between the deformation of B2 CuZr crystals and shear-banding for Cu-Zr-Zn BMG composites should be responsible for their ductility and obvious work hardening.

#### 4. Conclusions

In this paper,  $(\text{Cu}_{0.5}\text{Zr}_{0.5})_{100-x}\text{Zn}_x$  ( $x = 0, 1.5, 2.5, 4.5, 7, 10, \text{ and } 14$  at. %) bulk metallic glass (BMG) composites were fabricated. Based on the XRD and OM measurements, it was found that for the CuZr-based alloys with 0, 1.5, and 2.5 at. % Zn, the dominant phase is CuZr martensite together with minor B2 CuZr crystals and amorphous phase. With increasing Zn content from 4.5 at. % to 14 at. %, B2 CuZr and amorphous phases accompanying minor martensitic crystals can be obtained during quenching. All the investigated samples showed a relatively large compressive plastic strain and obvious work-hardening, which should result from the deformation-induced martensitic transformation within B2 CuZr crystals, the multiplication of shear bands in the glassy matrix, and the interactions between the deformation of B2 CuZr crystals and shear-banding.

#### Acknowledgments

The authors are grateful to B. Bartusch, B. Opitz, L. B. Bruno, M. Frey, S. Donath, and U. Wilke for technical assistance and enlightening discussions. D.Y. Wu and K.K. Song also thanks the support from the Fundamental Research Funds for the Central Universities on Northwestern Polytechnical University (3102014JCQ01090 and 3102015ZY078), the National Natural Science Foundation of

China (51501103, 51471135, 51171152 and 51301133) and the Fundamental Research Funds of Shandong University (1050501315006).

### Author Contributions

K.S. and C.C. conceived and designed the experiments, wrote and edited the manuscript, and contributed in all activities. D.W. performed XRD, OM, and SEM experiment. R.L., G.W., Y.W, F.W., F.D., Y.S., X.B., I.K., and J.E. helped finishing casting experiments, analyzing the results and revising the manuscript.

### Conflicts of Interest

The authors declare no conflict of interest.

### References

1. Schuh, C.A.; Hufnagel, T.C.; Ramamurty, U. Mechanical behavior of amorphous alloys. *Acta Mater.* **2007**, *55*, 4067–4109.
2. Greer, A.L.; Cheng, Y.Q.; Ma, E. Shear bands in metallic glasses. *Mater. Sci. Eng. R* **2013**, *74*, 71–132.
3. Yavari, A.R.; Lewandowski, J.J.; Eckert, J. Mechanical properties of bulk metallic glasses. *MRS Bull.* **2007**, *32*, 635–638.
4. Inoue, A.; Takeuchi, A. Recent Progress in Bulk Glassy Alloys. *Mater. Trans.* **2002**, *43*, 1892–1906.
5. Egami, T.; Iwashita, T.; Dmowski, W. Mechanical Properties of Metallic Glasses. *Metals* **2013**, *3*, 77–113.
6. Louzguine-Luzgin, D.V.; Louzguina-Luzgina, L.V.; Churyumo, A.Y. Mechanical properties and deformation behavior of bulk metallic glasses. *Metals* **2013**, *3*, 1–22.
7. Mu, J.; Zhu, Z.W.; Su, R.; Wang, Y.D.; Zhang, H.F.; Ren, Y. *In situ* high-energy X-ray diffraction studies of deformation-induced phase transformation in Ti-based amorphous alloy composites containing ductile dendrites. *Acta Mater.* **2013**, *61*, 5008–5017.
8. Pan, D.G.; Zhang, H.F.; Wang, A.M.; Hu, Z.Q. Enhanced plasticity in Mg-based bulk metallic glass composite reinforced with ductile Nb particles. *Appl. Phys. Lett.* **2006**, doi:10.1063/1.2423234.
9. Fu, H.M.; Wang, H.; Zhang, H.F.; Hu, Z.Q. *In situ* TiB-reinforced Cu-based bulk metallic glass composites. *Scr. Mater.* **2006**, *54*, 1961–1966.
10. Choi-Yim, H.; Conner, R.D.; Szuecs, F.; Johnson, W.L. Processing, microstructure and properties of ductile metal particulate reinforced  $Zr_{57}Nb_5Al_{10}Cu_{15.4}Ni_{12.6}$  bulk metallic glass composites. *Acta Mater.* **2002**, *50*, 2737–2745.
11. Oh, Y.S.; Kim, C.P.; Lee, S.; Kim, N.J. Microstructure and tensile properties of high-strength high-ductility Ti-based amorphous matrix composites containing ductile dendrites. *Acta Mater.* **2011**, *59*, 7277–7286.

12. Qiao, J.W.; Sun, A.C.; Huang, E.W.; Zhang, Y.; Liaw, P.K.; Chuang, C.P. Tensile deformation micromechanisms for bulk metallic glass matrix composites: From work-hardening to softening. *Acta Mater.* **2011**, *59*, 4126–4137.
13. Eckert, J.; Das, J.; Pauly, S.; Duhamel, C. Processing routes, microstructure and mechanical properties of metallic glasses and their composites. *Adv. Eng. Mater.* **2007**, *9*, 443–453.
14. Choi-Yim, H.; Johnson, W.L. Bulk metallic glass matrix composites. *Appl. Phys. Lett.* **1997**, *71*, 3808–3810.
15. Ma, H.; Xu, J.; Ma, E. Mg-based bulk metallic glass composites with plasticity and high strength. *Appl. Phys. Lett.* **2003**, *83*, 2793–2795.
16. Hofmann, D.C.; Suh, J.Y.; Wiest, A.; Duan, G.; Lind, M.L.; Demetriou, M.D.; Johnson, W.L. Designing metallic glass matrix composites with high toughness and tensile ductility. *Nature* **2008**, *451*, 1085–1089.
17. Wu, F.F.; Li, S.T.; Zhang, G.A.; Wu, X.F.; Lin, P. Plastic stability of metallic glass composites under tension. *Appl. Phys. Lett.* **2013**, doi:10.1063/1.4824879.
18. Qiao, J.W.; Zhang, Y.; Liaw, P.K.; Chen, G.L. Micromechanisms of plastic deformation of a dendrite/Zr-based bulk-metallic-glass composite. *Scr. Mater.* **2009**, *61*, 1087–1090.
19. Gargarella, P.; Pauly, S.; Song, K.K.; Hu, J.; Barekar, N.S.; Khoshkhoo, M.S.; Teresiak, A.; Wendrock, H.; Kühn, U.; Ruffing, C.; *et al.* Ti-Cu-Ni shape memory bulk metallic glass composites. *Acta Mater.* **2013**, *61*, 151–162.
20. Pauly, S.; Liu, G.; Wang, G.; Kühn, U.; Mattern, N.; Eckert, J. Microstructural heterogeneities governing the deformation of Cu<sub>47.5</sub>Zr<sub>47.5</sub>Al<sub>5</sub> bulk metallic glass composites. *Acta Mater.* **2009**, *57*, 5445–5453.
21. Song, K.K.; Pauly, S.; Zhang, Y.; Li, R.; Gorantla, S.; Narayanan, N.; Kühn, U.; Gemming, T.; Eckert, J. Triple yielding and deformation mechanisms in metastable Cu<sub>47.5</sub>Zr<sub>47.5</sub>Al<sub>5</sub> composites. *Acta Mater.* **2012**, *60*, 6000–6012.
22. Wu, Y.; Wang, H.; Wu, H.H.; Zhang, Z.Y.; Hui, X.D.; Chen, G.L.; Ma, D.; Wang, X.L.; Lu, Z.P. Formation of Cu-Zr-Al bulk metallic glass composites with improved tensile properties. *Acta Mater.* **2011**, *59*, 2928–2936.
23. Wu, Y.; Xiao, Y.H.; Chen, G.L.; Liu, C.T.; Lu, Z.P. Bulk Metallic Glass Composites with Transformation-Mediated Work-Hardening and Ductility. *Adv. Mater.* **2010**, *22*, 2770–2773.
24. Song, K.K.; Pauly, S.; Sun, B.A.; Tan, J.; Stoica, M.; Kühn, U.; Eckert, J. Correlation between the microstructures and the deformation mechanisms of CuZr-based bulk metallic glass composites. *AIP Adv.* **2013**, doi:10.1063/1.4789516.
25. Wu, F.F.; Chan, K.C.; Jiang, S.S.; Chen, S.H.; Wang, G. Bulk metallic glass composite with good tensile ductility, high strength and large elastic strain limit. *Sci. Rep.* **2014**, doi:10.1038/srep05302.
26. Liu, Z.Q.; Li, R.; Liu, G.; Su, W.H.; Wang, H.; Li, Y.; Shi, M.J.; Luo, X.K.; Wu, G.J.; Zhang, T. Microstructural tailoring and improvement of mechanical properties in CuZr-based bulk metallic glass composites. *Acta Mater.* **2012**, *60*, 3128–3139.
27. Liu, Z.Q.; Liu, G.; Qu, R.T.; Zhang, Z.F.; Wu, S.J.; Zhang, T. Microstructural percolation assisted breakthrough of trade-off between strength and ductility in CuZr-based metallic glass composites. *Sci. Rep.* **2014**, doi:10.1038/srep04167.

28. Li, C.J.; Tan, J.; Wang, G.; Bednarčík, J.; Zhu, X.K.; Zhang, Y.; Stoica, M.; Kühn, U.; Eckert, J. Enhanced strength and transformation-induced plasticity in rapidly solidified Zr-Co-(Al) alloys. *Scr. Mater.* **2013**, *68*, 897–900.
29. Pauly, S.; Das, J.; Bednarčík, J.; Mattern, N.; Kim, K.B.; Kim, D.H.; Eckert, J. Deformation-induced martensitic transformation in Cu-Zr-(Al, Ti) bulk metallic glass composites. *Scr. Mater.* **2009**, *60*, 431–434.
30. Song, K.K.; Pauly, S.; Zhang, Y.; Sun, B.A.; He, J.; Ma, G.Z.; Kühn, U.; Eckert, J. Thermal stability and mechanical properties of Cu<sub>46</sub>Zr<sub>46</sub>Ag<sub>8</sub> bulk metallic glass and its composites. *Mater. Sci. Eng. A* **2013**, *559*, 711–718.
31. Song, K.K.; Pauly, S.; Sun, B.A.; Zhang, Y.; Tan, J.; Kühn, U.; Stoica, M.; Eckert, J. Formation of Cu-Zr-Al-Er bulk metallic glass composites with enhanced deformability. *Intermetallics* **2012**, *30*, 132–138.
32. Wu, Y.; Song, W.L.; Zhang, Z.Y.; Hui, X.D.; Ma, D.; Wang, X.L.; Shang, X.C.; Lu, Z.P. Relationship between composite structures and compressive properties in CuZr-based bulk metallic glass system. *Chin. Sci. Bull.* **2011**, *56*, 3960–3964.
33. Sun, Y.F.; Wei, B.C.; Wang, Y.R.; Li, W.H.; Cheung, T.L.; Shek, C.H. Plasticity-improved Zr-Cu-Al bulk metallic glass matrix composites containing martensite phase. *Appl. Phys. Lett.* **2005**, doi:10.1063/1.2006218.
34. Song, K.K.; Pauly, S.; Zhang, Y.; Gargarella, P.; Li, R.; Barekar, N.S.; Kühn, U.; Stoica, M.; Eckert, J. Strategy for pinpointing the formation of B2 CuZr in metastable CuZr-based shape memory alloys. *Acta Mater.* **2011**, *59*, 6620–6630.
35. Kuo, C.N.; Huang, J.C.; Du, X.H.; Chen, Y.C.; Liu, X.J.; Nieh, T.G. Effects of V on phase formation and plasticity improvement in Cu-Zr-Al glassy alloys. *Mater. Sci. Eng. A* **2013**, *561*, 245–251.
36. Xie, M.T.; Zhang, P.N.; Song, K.K. Thermal Stability and Transformation-mediated Deformability of Cu-Zr-Al-Ni Bulk Metallic Glass Composite. *J. Mater. Sci. Technol.* **2013**, *29*, 868–872.
37. Song, K.K.; Pauly, S.; Wang, Z.; Kühn, U.; Eckert, J. Effect of TaW particles on the microstructure and mechanical properties of metastable Cu<sub>47.5</sub>Zr<sub>47.5</sub>Al<sub>5</sub> alloys. *Mater. Sci. Eng. A* **2013**, *587*, 372–380.
38. Javid, F.A.; Mattern, N.; Khoshkhoo, M.S.; Stoica, M.; Pauly, S.; Eckert, J. Phase formation of Cu<sub>50-x</sub>Co<sub>x</sub>Zr<sub>50</sub> ( $x = 0-20$  at. %) alloys: Influence of cooling rate. *J. Alloys Compd.* **2014**, *590*, 428–434.
39. Wu, D.Y.; Song, K.K.; Gargarella, P.; Cao, C.D.; Li, R.; Kaban, I.; Eckert, J. Glass-forming Ability, Thermal stability of B2 CuZr phase, and crystallization kinetics for rapidly solidified Cu-Zr-Zn alloys. *J. Alloys Compd.*, submitted for publication, 2015.
40. Seo, J.W.; Schryvers, D. TEM investigation of the microstructure and defects of CuZr martensite. Part I: Morphology and twin systems. *Acta Mater.* **1998**, *46*, 1165–1175.
41. Schryvers, D.; Firstov, G.S.; Seo, J.W.; Humbeeck, J.V.; Koval, Y.N. Unit cell determination in CuZr martensite by electron microscopy and X-ray diffraction. *Scr. Mater.* **1997**, *36*, 1119–1125.
42. Firstov, G.S.; Humbeeck, J.V.; Koval, Y.N. Peculiarities of the martensitic transformation in ZrCu intermetallic compound - potential high temperature SMA. *J. Phys. IV* **2001**, *11*, 481–486.

43. Kalay, I.; Kramer, M.; Napolitano R. Crystallization Kinetics and Phase Transformation Mechanisms in Cu<sub>56</sub>Zr<sub>44</sub> Glassy Alloy. *Metall. Mater. Trans. A* **2015**, *46*, 3356–3364.
44. Otsuka, K.; Wayman, C.M. *Shape Memory Materials*, 1st ed.; Cambridge University Press: Cambridge, UK, 1998; pp.1–49.
45. Wang, G.; Pauly, S.; Gorantla, S.; Mattern, N.; Eckert, J. Plastic Flow of a Cu<sub>50</sub>Zr<sub>45</sub>Ti<sub>5</sub> Bulk Metallic Glass Composite. *J. Mater. Sci. Tech.* **2014**, *30*, 609–615.
46. Pauly, S.; Gorantla, S.; Wang, G.; Kühn, U.; Eckert, J. Transformation-mediated ductility in CuZr-based bulk metallic glasses. *Nat. Mater.* **2010**, *9*, 473–477.
47. Han, Z.; Yang, H.; Wu, W.F.; Li, Y. Invariant critical stress for shear banding in a bulk metallic glass. *Appl. Phys. Lett.* **2008**, doi:10.1063/1.3048869.
48. Zhang, Z.F.; Eckert, J.; Schultz, L. Difference in compressive and tensile fracture mechanisms of Zr<sub>59</sub>Cu<sub>20</sub>Al<sub>10</sub>Ni<sub>8</sub>Ti<sub>3</sub> bulk metallic glass. *Acta Mater.* **2003**, *51*, 1167–1179.
49. Sun, B.A.; Wang, W.H. The fracture of bulk metallic glasses. *Prog. Mater. Sci.* **2015**, *74*, 211–307.
50. Argon, A.S.; Salama, M. The mechanism of fracture in glassy materials capable of some inelastic deformation. *Mater. Sci. Eng.* **1976**, *23*, 219–230.
51. Sun, B.A.; Tan, J.; Pauly, S.; Kuhn, U.; Eckert, J. Stable fracture of a malleable Zr-based bulk metallic glass. *J. Appl. Phys.* **2012**, doi:10.1063/1.4767327.
52. Deibler, L.A.; Lewandowski, J.J. Model experiments to mimic fracture surface features in metallic glasses. *Mater. Sci. Eng. A* **2010**, *527*, 2207–2213.
53. Lewandoski, J.J.; Greer, A.L. Temperature rise at shear bands in metallic glasses. *Nat. Mater.* **2006**, *5*, 15–18.
54. Wu, F.F.; Chan, K.C.; Li, S.T.; Wang, G. Stabilized shear banding of ZrCu-based metallic glass composites under tensile loading. *J. Mater. Sci.* **2014**, *49*, 2164–2170.
55. Tong, X.; Wang, G.; Yi, J.; Ren, J.L.; Pauly, S.; Gao, Y.L.; Zhai, Q.J.; Mattern, N.; Dahmen, K.A.; Liaw, P.K.; *et al.* Shear avalanches in plastic deformation of a metallic glass composite. *Int. J. Plast.* **2016**, *77*, 141–155.
56. Song, K.K. Synthesis, microstructure, and deformation mechanisms of CuZr-based bulk metallic glass composites. In *Doctoral Thesis Work*; TU Dresden: Dresden, Germany, 2013.